Grayscale lattice Boltzmann model for multiphase heterogeneous flow through porous media

Gerald G. Pereira
CSIRO Computational Modelling, Private Bag 10, Clayton South, 3169, Australia
(Received 21 October 2015; revised manuscript received 10 February 2016; published 6 June 2016)

The grayscale lattice Boltzmann (LB) model has been recently developed to model single-phase fluid flow through heterogeneous porous media. Flow is allowed in each voxel but the degree of flow depends on that voxel's resistivity to fluid motion. Here we extend the grayscale LB model to multiphase, immiscible flow. The new model is outlined and then applied to a number of test cases, which show good agreement with theory. This method is subsequently used to model the important case where each voxel may have a different resistance to each particular fluid that is passing through it. Finally, the method is applied to model fluid flow through real porous media to demonstrate its capability. Both the capillary and viscous flow regimes are recovered in these simulations.

DOI: 10.1103/PhysRevE.93.063301

I. INTRODUCTION

The lattice Boltzmann method (LBM) has been developed over the past thirty years and has proven to be a numerically efficient and accurate method to model fluid flow in confined, topologically complex geometrical domains. LBM does not directly solve the Navier-Stokes equations but rather the Boltzmann transport equation. Through a Chapman-Enskog expansion it can be shown the solution obtained with LBM is equivalent to that which would have been obtained from a direct solve of the Navier-Stokes equation [1,2]. LBM is now commonly applied to determine the permeability of complex porous media such as carbonates, shales, and other reservoir rocks (e.g., [3–13]). The inputs for these computations is a digital representation of the porous medium, which usually comes from CT scans. Here each voxel corresponds to a solid region (not available for fluid flow) or void region (available for fluid flow). Suitable boundary conditions are applied at boundaries between solid and void voxels, to account for a no-slip boundary condition. Steady-state fluid velocity distributions can then be obtained from this LBM solution to give an estimate for the medium's permeability. We refer to such a model as a black-white (BW) model.

Typical resolutions of CT scans are of the order of 1–10 μm. However, in many mineral rocks, the grain size is much smaller than this—maybe of the order of 10–100 nanometers or so. This means a given voxel will contain both solid and pore regions. Moreover, rocks are constituted of more than one material and these materials can have different surface boundary conditions, which will affect resistance to fluid flow. This discussion implies a BW model cannot be applied to CT scans for a range of heterogeneous rocks, which are of current interest to those in the petroleum and natural gas industries. Rather a model, which allows for differing amounts of flow depending on that voxel's (fractional) solid constitution, is required. This has been the motivation behind the development of so-called grayscale LBM models [14–22].

LBM is a class of cellular automata, which is solved on a regular lattice (usually simple-cubic in three dimensions). On each lattice vertex or node, where the location of each node is the center of a voxel from the CT scan, a set of fluid particle distribution functions is defined. There are Q distribution functions defined on each node. LBM then consists of three main steps. The first step is called streaming, in which all fluid packets (distributions) are moved to adjacent sites. This streaming can be correlated to the normal advection of fluid. The second step is called bounce back, which accounts for fluid-solid boundary conditions. Here fluid packets at boundary nodes are reversed in direction (or more complicated half-way bounce back or interpolation boundary conditions may be implemented). The final step in LBM is a collision step where fluid packets converging on a given node are redistributed according to the Maxwell distribution. The LBM method then consists of iterating these three steps (in a pseudo-time-stepping manner) to give a solution. This procedure works well for a BW model [7,11]. In the grayscale models there are no fluid-solid boundaries, as such. All voxels are allowed a certain degree of flow. This can be related to the solid fraction in that voxel, but other effects such as tortuosity, topology, mineral content etc can be included into the model to contribute to the voxel's resistance to flow. To account for this a partial bounce-back rule is imposed on each voxel [14–18]. This means at each voxel a certain fraction of fluid packets (which were streamed into a node) will be bounced back. We denote the fraction of fluid packets, which are bounced back at a node by n_s ($0 \leqslant n_s \leqslant 1$) and each node can have a different n_s value.

The single-phase grayscale model, just described, has previously been implemented to simulate (single-phase) fluid flow in real rocks, which are made up of a number of different minerals [23]. The mineral content for each voxel was extracted using a data constrained modeling (DCM) methodology [24] and then these fractional contents were used in combination with a simple rule, relating the void and calcite fractions to the n_s value for each voxel. Not only were the results numerically stable but they were also physically realistic, which makes this method a suitable candidate for extensions to multiphase fluid flow studies. It is noted here this method can also be used to upscale permeability to larger sample sizes, as long as an effective fluid resistance can be determined for individual elements.

Multiphase fluid flow (e.g., oil and water or gas and oil) is of utmost importance in the petroleum industry. Two or three phase relative permeabilities are notoriously difficult to obtain experimentally. A numerical method that can calculate these permeabilities would be of significant benefit. With this

in mind we now consider applying the grayscale model to multiphase fluid flow. Multiphase LBM models with BW voxels have already been developed. The multiphase model we use is a version of the original Shan-Chen model [25] but with an extended range for the interaction term, a more accurate forcing scheme, as well as a multirelaxation time scheme [26–29]. In keeping with previous work we refer to it as the pseudopotential LBM model [27,30] (so as to differentiate from the original Shan-Chen model). In this study we combine this multiphase model with the single-phase grayscale model to yield a multiphase, grayscale LBM method.

The structure of this paper is as follows: In the next section we briefly describe the multiphase grayscale LBM model, starting of with a description of the single-phase grayscale scheme based on the work of Walsh *et al.* [18]. We then describe how to extend the single-phase model to multiple, immiscible phases. Once the we have outlined our algorithm, we determine its validity by comparing it with test cases, where theoretical results are known. Finally, we apply the method to model immiscible flow in sample porous media.

II. GRAYSCALE LATTICE BOLTZMANN MODEL

Grayscale lattice Boltzmann models allow for fluid flow at every lattice node, but to varying extent depending on the fluid resistivity of the corresponding voxel. These grayscale LBM schemes have been developed over the last 20 years or so [14–16,18,20,23]. The aim of this paper is to develop a grayscale model for multiphase, immiscible flow. This is most easily understood by first describing the single-phase grayscale model, which has been established and validated [16,18,20,23].

A. Single-phase grayscale model

In dealing with flow of a single fluid one set of particle distribution functions is defined, i.e., $f(\mathbf{r},\mathbf{u},t)$, which denotes the distribution of particles traveling with a particular velocity $\mathbf{u}$ at lattice node $\mathbf{r}$ at time t. The geometrical domain consists of a three-dimensional, simple-cubic lattice and the D3Q19 model, which consists of 18 possible vector directions in which a particle may move ($\mathbf{e}_i$) plus the null vector, is implemented. At each time step these eighteen distribution functions at each node, are propagated to adjacent nodes in the appropriate $\mathbf{e}_i$ direction and subsequently solve the following LBM equation at node i:

$$f_i(\mathbf{r}+\mathbf{e}_i\Delta t,t+\Delta t)-f_i(\mathbf{r},t)=\Omega(f,\mathbf{r},t). \tag{1}$$

In the single relaxation time (SRT) scheme the collision operator is given by

$$\Omega(f,\mathbf{r},t)=-\frac{\left[f_i(\mathbf{r},t)-f_i^{\mathrm{eq}}(\mathbf{r},t)\right]}{\tau}. \tag{2}$$

In Eq. (2), τ represents a relaxation time and it can be shown to be related to kinematic viscosity via $\nu=c_s^2(\tau-1/2)$, where c_s is the sound speed and equal to $1/\sqrt{3}$. The pressure is given by $P=c_s^2\rho$. The term f_i^{eq} is the equilibrium Maxwell distribution given by [1,2]

$$f_i^{\mathrm{eq}}=w_i\rho\left[1+\frac{\mathbf{e}_i\cdot\mathbf{u}^{\mathrm{eq}}}{c_s^2}+\frac{(\mathbf{e}_i\cdot\mathbf{u}^{\mathrm{eq}})^2}{2c_s^4}-\frac{\mathbf{u}^{\mathrm{eq}}\cdot\mathbf{u}^{\mathrm{eq}}}{2c_s^2}\right], \tag{3}$$

where w_i are weights, which are well known [1] for the given D3Q19 model.

Macroscopic parameters such as density and velocity can be obtained from moments of distribution functions as follows:

$$\rho=\sum_i f_i \quad\text{and}\quad \rho\mathbf{u}=\sum_i f_i\mathbf{e}_i. \tag{4}$$

To model forces, such as body forces such as gravity or even surface forces between different fluid phases, we add an explicit forcing term to the LB equation (1). This forcing term is defined as [31]

$$\mathcal{F}_i=\frac{\mathbf{F}\cdot(\mathbf{e}_i-\mathbf{u}^{\mathrm{eq}})}{\rho c_s^2}f_i^{\mathrm{eq}}, \tag{5}$$

where $\mathbf{F}$ is the force. The macroscopic velocity is updated in this case to $\rho\mathbf{u}=\sum_i f_i\mathbf{e}_i+\mathbf{F}/2$ and $\mathbf{u}^{\mathrm{eq}}=\mathbf{u}$. This implementation of the applied force is not only accurate but exhibits correct time evolution of the flow.

The SRT method, although relatively simple to implement, suffers from a few well-documented problems. In the context of porous media applications one of the main issues is that the flow field and hence the permeability is viscosity dependent. However, physically this should not be the case. As a result a more complicated model, which overcomes these deficiencies needs to be implemented and is known as the multirelaxation time (MRT) scheme [32].

Here a linear transformation (matrix) $\underline{\underline{\mathbf{M}}}$ is chosen so that the moments

$$m_i(\mathbf{r},t)=\sum_j M_{ij}f_j(\mathbf{r},t), \tag{6}$$

represent the hydrodynamic modes of the problem. The collision operator in Eq. (2) is replaced by

$$\begin{aligned}\Omega(f,\mathbf{r},t)&=-\left[\underline{\underline{\mathbf{M}}}^{-1}\cdot\underline{\underline{\mathbf{S}}}\cdot\underline{\underline{\mathbf{M}}}\left(f_i-f_i^{\mathrm{eq}}\right)\right]\\&=-\left[\underline{\underline{\mathbf{M}}}^{-1}\cdot\underline{\underline{\mathbf{S}}}\cdot\left(m_i-m_i^{\mathrm{eq}}\right)\right].\end{aligned} \tag{7}$$

The various moments (m and m_{eq}) are given in detail in d'Humieres *et al.* [32] with the important ones for this study being the density (m_0) and fluid momenta (m_3, m_5, m_7). $\underline{\underline{\mathbf{S}}}$ is a diagonal matrix given by $(0,s_1,s_2,0,s_4,0,s_4,0,s_4,s_9,s_{10},s_9,s_{10},s_{13},s_{13},s_{13},s_{16},s_{16},s_{16})$. The precise (numerical) values are chosen for optimal numerical stability [32]. The kinematic viscosity in the model is $\nu=(1/s_9-1/2)/3$. In addition, nineteen definitions are given for the moments of an equilibrium distribution such that the Chapman-Enskog expansion ensures that the Navier-Stokes set of equations is solved [32]. The equilibrium distribution and therefore its moments depend only on the fluid density, three components of the fluid momentum and speed of sound. The collision operator is built such that each distribution moment will relax towards the equilibrium distribution moments. The specific values of the relaxations parameters in the D3Q19 MRT model that we use are as follows:

$$\begin{aligned}(s_1,\ldots,s_{19})=(&0,1.19,1.4,0,1.2,0,1.2,0,1.2,1/\tau,1.4,\\&1/\tau,1.4,1/\tau,1/\tau,1/\tau,1.98,1.98,1.98).\end{aligned} \tag{8}$$

In the grayscale LBM method at each node a certain fraction of the fluid packets that are streamed into that node are bounced back. This fraction of fluid packets, which are bounced back

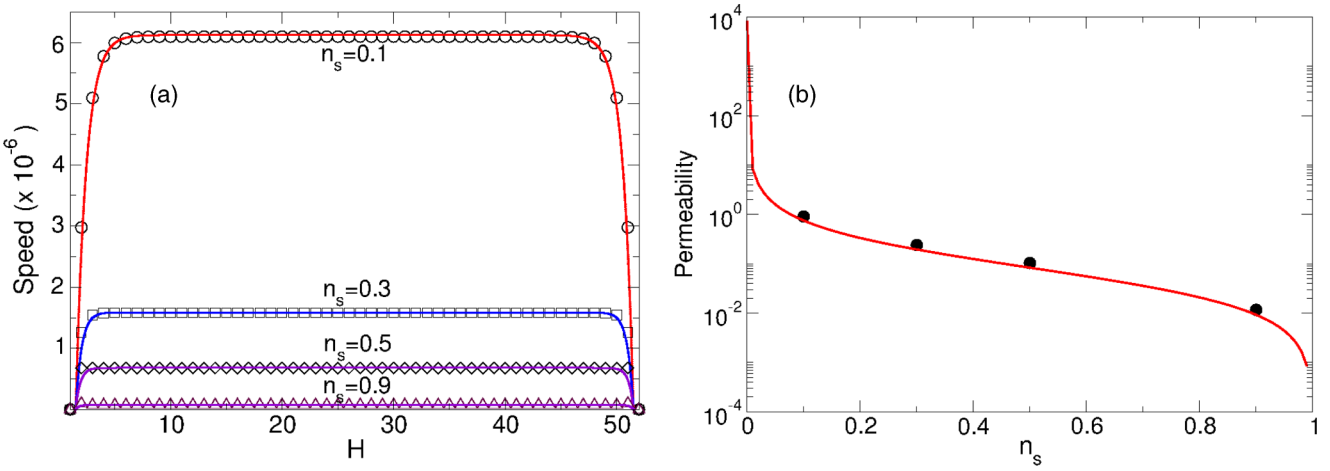

FIG. 1. (a) Comparison between Brinkman flow analytic solution and LB grayscale model for single-phase flow with a body force $G = 10^{-6}$. Symbols are LB results and curves are analytic solutions. Circles correspond to $n_s = 0.1$, squares to $n_s = 0.3$, diamonds to $n_s = 0.5$ and triangles to $n_s = 0.9$. (b) Permeability comparison between theory (curve) and LB simulations (circles).

at any given node is given by n_s and so Eq. (1) is replaced by

$$f_i(\mathbf{r}+\mathbf{e}_i\Delta t, t+\Delta t) = (1-n_s)f_i(\mathbf{r},t) - (1-n_s)\Omega(f,\mathbf{r},t) + (1-n_s)\mathcal{F}_i + n_s\hat{f}_i(\mathbf{r},t). \quad (9)$$

The last term with the hat on the distribution function indicates the distribution function to be added is in the opposite direction to i. The parameter n_s is between 0 and 1 and can be related to voxel composition and/or topological properties (among other things). The macroscopic velocity is now

$$\rho\mathbf{u} = (1-n_s)\left(\sum_i f_i\mathbf{e}_i + \mathbf{F}/2\right). \quad (10)$$

Equation (9) represents the grayscale LB model of Walsh *et al.* [18]. It has previously been validated for test cases such as the Brinkman flow equation [18,33,34] as well as giving qualitatively reasonable results on real samples [23] using pressure boundary conditions to drive the fluid.

We now compare our code results of this model, using a body force to drive the fluid (e.g., for a gravity driven flood), with the Brinkman model. The Darcy-Brinkman equation models laminar flow through a channel, which has a nonzero resistance (or drag). It is given by

$$\nabla^2 u - \left(\frac{\phi}{\nu_B}\right)u = \frac{1}{\rho\nu_B}G, \quad (11)$$

where ϕ is the resistance to flow in some local region, ν_B is the Brinkman viscosity and G is the body force. The solution of this equation (flow is in the x direction, the channel has width H in the y direction and is periodic in the z direction) is

$$u(y) = -\frac{G}{\phi\rho}\left[1 - \frac{\cosh r(y-H/2)}{\cosh(rH/2)}\right], \quad (12)$$

where $r \equiv \sqrt{\phi/\nu_B}$ and $\phi = 2n_s$. Figure 1(a) shows a comparison between the single-phase LB solution at different n_s values (from our code) compared with the Brinkman solution (12). The comparison shows good overall agreement over a wide range of n_s values. (Note that LB results are presented in dimensionless units.) The permeability can be calculated from the average channel speed together with Darcy's Law, i.e., $k = \nu\langle\rho u\rangle/G$ and shows good agreement [see Fig. 1(b)] with the theoretical prediction derived in Walsh *et al.* [18]:

$$k = \frac{(1-n_s)\nu}{2n_s}. \quad (13)$$

The multiphase grayscale LBM algorithm is now developed as an extension of this single-phase method.

B. Multiphase grayscale lattice Boltzmann model

The multiphase grayscale model combines the single-phase grayscale model (just described) with multiphase immiscible flow for BW models [25–28,31]. We begin with a description of a multiphase BW model and then extend it to a grayscale model. For n immiscible phases we now define n sets of distributions functions, which represent each immiscible phase: $f^1(\mathbf{r},\mathbf{u},t)\ldots f^n(\mathbf{r},\mathbf{u},t)$. For each phase we solve the LB equation at node i. So for the kth phase (where $k \in 1,\ldots,n$) we need to solve the LB equation:

$$f_i^k(\mathbf{r}+\mathbf{e}_i\Delta t, t+\Delta t) - f_i^k(\mathbf{r},t) = \Omega^k(f_k,r,t) + \mathcal{F}_i^k, \quad (14)$$

where $\mathcal{F}_i^k$ contains all additional forces including surface tension (as we shall see below), gravity, etc. The collision operators, either for the SRT or MRT schemes, follow a similar form to that given for single-phase flow with the exception that each phase has its own relaxation time (or $\underline{\underline{\mathbf{S}}}$ matrix). Values for various macroscopic variables such as density, momentum flux, etc. follow almost analogously from the single-phase equations, using the appropriate distribution function for each phase [25,26,28,30].

To model immiscibility between phases the pseudopotential model [26–28] is used, which is an extension of the original Shan-Chen model [25]. The Shan-Chen model employs nearest-neighbor interaction potentials to model the interactions between components. In a sense this follows physical reality at the microscopic level where molecules interact via short-range Lennard-Jones-type potentials. In the original Shan-Chen model [25] only lattice nodes, which are nearest neighbors (i.e., separated by 1 lattice spacing), are

coupled together and these couplings are incorporated into a surface force at each lattice node.

One of the issues with this nearest-neighbor implementation is that it leads to large spurious currents, which are a numerical artifact of using a a small and discrete set of neighbors to approximate what should really be a continuum set of force vectors. These numerical artifacts, if not reduced to a minimum, will lead to large numerical instabilities. To reduce these numerical instabilities it has been found [26–28] that extending the range of the pseudopotential leads to a significant reduction (up to 1000 times) of these spurious currents. The range of pseudopotential can in principal go to infinity but this of course comes at a computational cost. Both sixth-order (including all neighbors less than or equal to 2 units away) and eighth-order (including all neighbors less than or equal to $\sqrt{8}$ units away) pseudopotentials have been utilized in this work. This increases the number of neighbors to be sampled from 6 (Shan-Chen) to 32 (sixth order) to 64 (eighth order), but greatly enhances the numerical stability of the method.

The fluid-fluid interaction for phase k at lattice node $\mathbf{r}$ is given by

$$\mathbf{F}_k(\mathbf{r}) = \rho_k(\mathbf{r}) \sum_{k' \neq k} g_{kk'} \sum_i w(|\mathbf{e}_i|^2) \rho_{k'}(\mathbf{r} + \mathbf{e}_i)\mathbf{e}_i, \tag{15}$$

where $g_{kk'}$ is the interaction potential (or coupling parameter) between dissimilar components. In principal, the phases can also have different molecular mass, which we denote as m_k. The weights w depend on the separation between interacting nodes and complete tables of weights for sixth- and eighth-order pseudopotentials are given in Sbragaglia *et al.* [27]. Note, we assume the coupling is zero for similar components. The additional term $\mathcal{F}_i^k$ in Eq. (14) is given by [31]

$$\mathcal{F}_i^k = \frac{\mathbf{F}_k \cdot (\mathbf{e}_i - \mathbf{u}^{\mathrm{eq}})}{\rho_k c_s^2} f_i^{k,eq}. \tag{16}$$

The equilibrium velocity in Eq. (16) is now a combined velocity and to satisfy momentum conservation must be

$$\mathbf{u}^{\mathrm{eq}} = \frac{\sum_k s_9^k \rho_k \mathbf{u}_k}{\sum_k s_9^k \rho_k}. \tag{17}$$

The pressure in this model is given by the equation of state

$$P = c_s^2 \sum_k \rho_k + \frac{1}{2} \sum_{kk'} g_{kk'} \rho_k \rho_{k'} \tag{18}$$

and the phase velocities are

$$\rho_k \mathbf{u}_k = \sum_i m_k f_i^k \mathbf{e}_i + \mathbf{F}_k/2. \tag{19}$$

The final step in developing a multiphase grayscale algorithm is to incorporate the effect of voxel resistivity. To do this we essentially use Eq. (9) but now apply it to each of the k phases. We assume that the resistivity of a particular voxel to fluid flow is different for each phase, so that we can have up to k different n_s values for each voxel. Physically this may be the case if there are different materials in a voxel, which have different (surface) interactions with different fluids. Thus the multiphase gray LB evolution equation becomes

$$f_i^k(\mathbf{r}+\mathbf{e}_i\Delta t, t+\Delta t) = \left(1-n_s^k\right) f_i(\mathbf{r},t) - \left(1-n_s^k\right)\Omega(f^k,\mathbf{r},t) + \left(1-n_s^k\right)\mathcal{F}_i^k + n_s^k \hat{f}_i^k(\mathbf{r},t). \tag{20}$$

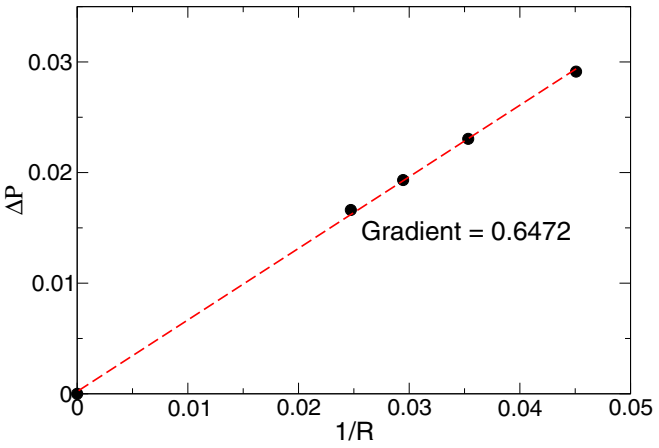

FIG. 2. Pressure difference between inside and outside of droplet versus inverse radius for $g_{AB} = 1.33$. The best fit line (dashed) has a gradient of 0.6472.

The macroscopic velocity for each phase is defined similarly to Eq. (10) with suitable n_s^k, f^k and $\mathbf{F}^k$ values for each component.

C. Calibration of microscopic $g_{kk'}$ to macroscopic surface tension

The microscopic interaction parameter, $g_{kk'}$, needs to be calibrated to macroscopic surface tension and (if required) contact angle measurements. This calibration process also validates the multiphase LBM code since it yields an interface between two immiscible phases k and k'. To obtain the relationship between the microscopic parameter, $g_{kk'}$, and macroscopic variables we use the Young-Laplace equation

$$\Delta P = \frac{2\gamma}{R}. \tag{21}$$

Here ΔP is the pressure difference across the fluid interface, γ is the macroscopic surface tension and R is a droplet radius.

To obtain γ we begin with two phases A and B (B phase surrounds A phase) in a cubical geometry. A number of different sized cubes are tested and these cubical droplets quickly relax to spheres of different radius. We measure the pressure difference between the interior and exterior of the droplet to give $\Delta P \equiv P_{\mathrm{in}} - P_{\mathrm{out}}$ and using Eq. (18) for P_{in} and P_{out}. This plot is shown in Fig. 2 where we used a g_{AB} value of 1.33. The surface tension is extracted from the gradient of this line and is 0.3236.

We have previously applied the BW, multiphase LBM method to scenarios such as multiphase fluid flow through packed beds as well as real porous media and have achieved physically realistic results [29]. The method shows good numerical stability for a relatively wide range of surface tensions and viscosity ratios. Thus, we now proceed to assessing the validity of the newly developed grayscale, multiphase LBM method. After this validation the method is applied to some more realistic scenarios to demonstrate its capability.

III. MODEL PERFORMANCE AND DISCUSSION

To validate the new multiphase grayscale model we consider multiphase flow through a channel. We then consider

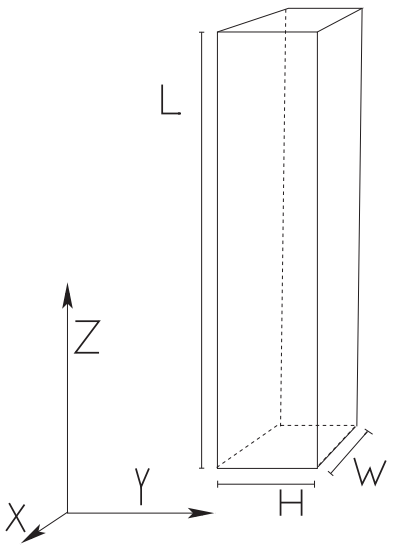

FIG. 3. Schematic of geometry of long, slender channel, which is used for test cases in this section ($W < H \ll L$). The body force is applied in the positive z direction.

the effect of a solid-fluid interaction on the flow and then through and around semipermeable tows. Finally, multiphase flow through a real, heterogeneous porous medium.

For the simulations presented here relaxations of $\tau_A \equiv 1/(s_9)_A = 1$ and $\tau_B \equiv 1/(s_9)_B = 2$ are used, which give viscosities of $\nu_A = 1/6$ and $\nu_B = 1/2$ and other parameters for the multi-relaxation model are given in Eq. (8). The interaction potential (or coupling parameter) is $g_{AB} = 1.33$ and the mass of the phases are $m_A = 2$ and $m_B = 1$. For the first three sets of tests below, a long, slender channel geometry is utilized, i.e., $W \times H \times L$, where $W < H \ll L$ (shown schematically in Fig. 3). A body force is placed in the z direction to drive the fluid motion. Precise values for parameters such as body forces, lattice dimensions, and n_s are varied between simulations and given below.

A. Multiphase channel flow

In this test two-phase channel flow is modeled, i.e., phase A displacing phase B in a narrow channel with periodic boundary conditions in the x and z directions. At $y = 1$ and $y = H + 1$ an n_s value of 1 is used for both phases and for the rest of the channel the n_s value is varied from zero up to 0.7, between different simulations. The n_s value is kept the same for both phases in these simulations. Recall a larger n_s value indicates a large resistance to flow, so that $n_s = 1$ in the y boundaries indicates no flow normal to these boundaries. The channel is filled with phase B except for a smaller region at the lower end (between $z = 1$ to $z = 30$), which is filled with phase A. A body force is applied in the positive z direction to drive the fluids. For all the following cases, we have $W = 21$, $H = 41$. For the initial case where $n_s = 0$ within the channel, we use a channel length of $L = 301$, which is double the length for the following five cases (where $L = 151$). For $n_s = 0$ we use a body force of 6.8×10^{-5}, which is applied in the positive z direction. This case corresponds to multiphase Pouseille flow through a channel where the velocity profile is parabolic. Figure 4(a) shows the channel flow at the LB time of 550. The two dark orange stripes on each side of the channel (near the bottom) indicate where the A phase began. Because of the no-slip boundary condition on these edges, fluid is stationary here. As a consequence, the A phase, which was initially at these edges remains for the duration of the simulation. The interface profile between phases is parabolic in shape but highly curved.

For the five cases of $n_s = 0.05, 0.1, 0.3, 0.5$, and 0.7 we use an appreciably larger body force of 6.8×10^{-3}. A much larger body force is required because the drag on the fluid induced by the increased resistance of the medium (from a nonzero n_s value) is large enough to prevent any appreciable flow for much smaller body forces. (Note that if we had used such a large body force for the $n_s = 0$ case, it would have resulted in speeds much larger than the sound speed, which is not physically sensible for laminar flow in a porous medium.) The shape of the interface between phases results from a combination of surface tension and fluid drag. As the n_s value is increased from zero, the first thing we notice is that the interface profile becomes much flatter, in the middle of the channel and less curved overall. This is in agreement with the velocity profiles shown in Fig. 1. The other noticeable aspect of the interface is that the tail of the A phase [marked in Fig. 4(c)] diminishes in length as n_s increases. For the largest n_s value of 0.7 [Fig. 4(f)] the tail is nonexistent, with only a slight bow in the interface (at the back end). The long tail (for small n_s) is due to the zero slip condition on the boundaries (i.e., $y = 1$ and $H + 1$). As n_s increases the difference in drag between the boundaries and the interior of the channel diminishes and consequently the tails diminish in length.

According to Darcy's law the average (channel) velocity in a porous medium (for laminar flow) is given by

$$\langle V_x \rangle = \frac{Gk}{\nu\rho}, \tag{22}$$

where G is the body force and k is the permeability. So the average channel velocity is proportional to the permeability. In the grayscale models [18] the permeability is related to n_s via Eq. (13), so that the average velocity along the channel is

$$\langle V_x \rangle = \frac{G(1 - n_s)}{2n_s\rho}. \tag{23}$$

We can determine the average A phase velocity in the channel by tracking the interface as a function of time. Doing this for the five different simulations, at the same G value, and plotting the average velocity as a function of n_s gives Fig. 5. Note, we have also added the $n_s = 1$ value, which gives zero channel speed [see Eq. (10)]. We obtain a linear relationship between $\langle V_x \rangle$ and $(1 - n_s)/n_s$, in agreement with Eq. (23). We estimate the average A phase density to be 0.65, which is obtained by averaging densities in the middle of the A phase drop, well away from the interface over the five cases. Using the gradient of the graph and the A phase average density of 0.65 we predict the body force is 6.9×10^{-3}, which agrees well with the actual body force we used for these five cases.

B. Solid-fluid interaction

Typical porous media consists of different minerals, which may have different resistance to flow for different fluids (e.g., surface effects depend on the wettability of a particular

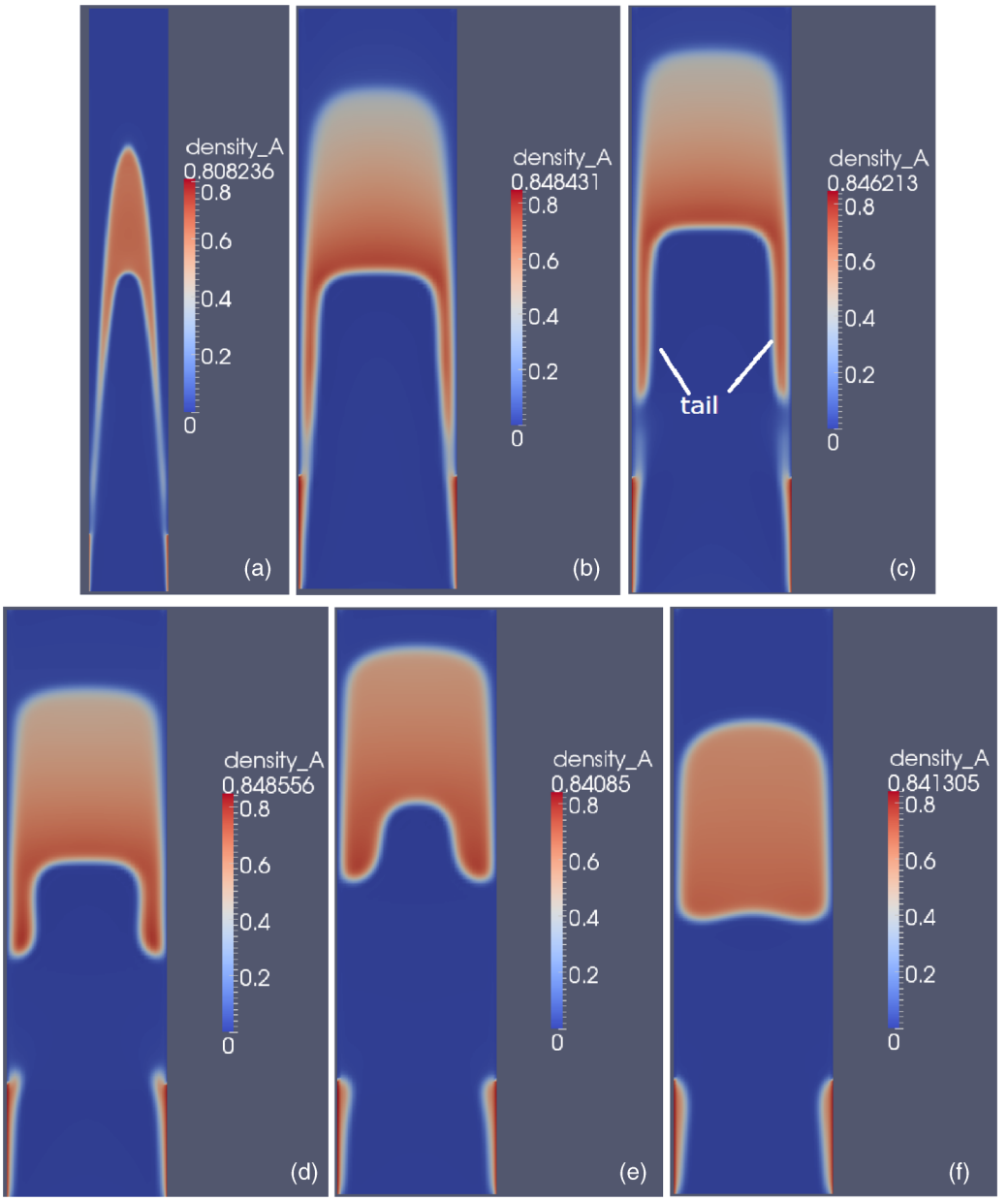

FIG. 4. Multiphase channel flow for a variety of n_s values (times given are the times taken by the A phase droplet to move from the bottom to the position shown). (a) $n_s = 0$, $t = 550$, (b) $n_s = 0.05$, $t = 900$, (c) $n_s = 0.1$, $t = 2200$, (d) $n_s = 0.3$, $t = 12100$, (e) $n_s = 0.5$, $t = 51000$, (f) $n_s = 0.5$, $t = 51000$. In (a) channel length is double and the body force is 100 times larger than in the other five cases. In (c) we mark the tails of A phase, which we refer to in the text.

mineral). To model such an effect, we require the n_s values to be different for the different fluid phases. This we now consider the effect of using different n_s values for the two phases. Consider the case where $n_s^A = 0.0$ and $n_s^B = 0.3$ and we use similar channel dimensions to above. However, we fill half the channel ($z = 1$ to $L/2$) with the A phase and other half with the B phase. Again a body force of 6.8×10^{-3} is applied in the positive z direction. With this configuration there is larger resistance to flow for the B phase. Figure 6 gives three snapshots of the displacement of B phase by the A phase. The interface between phases is highly curved and resembles the interface in Fig. 4(a), where n_s was zero (for both phases). Since the A phase is being forced through the B phase it is this phase that governs the shape of the interface. This shape resembles a parabolic (Pouseille-like) profile.

On the other hand, when $n_s^A = 0.3$ and $n_s^B = 0.0$ (see Fig. 7) the shape of the interface is now much rounder since the A phase now has a high resistance to flow. In both cases, as one moves well back from the interface, the whole of the channel is filled with that particular phase. This means in the region where the A phase is the majority phase only a thin film of the B phase remains adjacent to the solid edges, which has zero velocity, to satisfy the no-slip boundary condition. The times required for the tip of the A phase to reach the end of the channel (i.e., $z = 151$), which is a distance of 75 LB grid spacings is 500 LB time units, which gives an average speed of 0.15. In comparison, when $n_s^A = 0.0$ and $n_s^B = 0.3$ the time

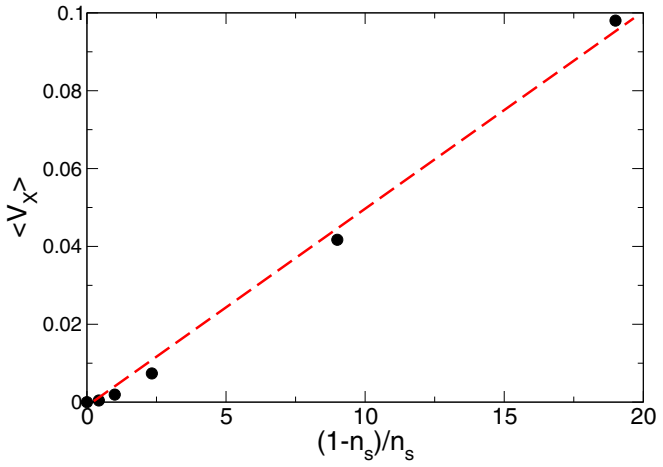

FIG. 5. Plot of the average channel velocity of phase A versus $(1-n_s)/n_s$. Solid circles are from the LB simulations while the dashed line is a best fit with gradient of 5.29 $\times 10^{-}3$.

required for the interface tip to reach the end of the channel is 280 LB time units yielding an average speed of 0.27. The higher speed for smaller n_s^A corresponds to the observation that A phase governs the interface shape since it is the phase being driven through the channel.

Simulations for other pairings of n_s^A and n_s^B such as 0.5 and 0.1 (and vice versa) have been carried out and the results correspond in general to the simulations presented above. (Average channel speeds for all the combinations simulated are shown in Table I.) In summary, the capability to have different voxel resistivity for each phase is a physically important scenario. Our new method has been demonstrated to be capable of modeling this situation yielding a numerically stable and physically realistic solution.

1. Capillarity

If a particular mineral has an attractive intermolecular attraction to a particular fluid, the fluid will tend to spread over the solid surface. This causes a reduction in the contact angle to partial or complete wetting conditions. This attractive interaction leads to capillary rise, i.e., rise of a fluid column in narrow capillaries or tubes. Our present method can model this situation, but it should be noted in the general grayscale formulation a lattice node may not represent the exact pore-scale morphology (since the resolution of the digital image is larger than the actual pore-scale fine structure). The level of approximation in the calculation of the solid-fluid interaction will be as good as this resolution. (Of course this level of approximation is the same as in grayscale single-phase fluid flow.)

The interaction between the solid (s) and phase k is defined as:

$$\mathbf{F}_{ks} = \rho_k(\mathbf{r}) g_{ks} \sum_i w(|\mathbf{e}_i|^2) s_s(\mathbf{r}+\mathbf{e}_i)\mathbf{e}_i, \qquad (24)$$

where g_{ks} is the coupling parameter (between fluid phase k and solid) and $s_s(\mathbf{r})$ is the solid fraction at $\mathbf{r}$ and $0 \leqslant s_s \leqslant 1$. The weighting function $w(|\mathbf{e}_i|^2)$ and range of the sum are the same as used in Eq. (15). This formulation reduces to the conventional BW multiphase model (when s_s is either zero or one) [26,29,30] yielding a contact angle between zero and π radians, depending on the values of g_{ks}.

To model the effect of capillarity we consider a channel with solid walls at $y = 0$, $y = H$, $z = 1$ and $z = L$ (with $W = 21$, $H = 41$, and $L = 151$) and periodic in the x direction. Since the walls are assumed solid we assign both $n_s = 1$ and $s_s = 1$ along these walls. We assume the remainder of the channel is void so that both $n_s = 0$ and $s_s = 0$. The channel is filled with B phase except for a small region at the lower end (between $z = 0$ to $z = H/3$). We use $g_{As} = 0$ and $g_{sB} = 1.33$, which results in the A phase preferring the side walls (and consequently it makes a contact angle of less than $\pi/2$ radians with these walls). This means in the absence of any other forces, the A phase would prefer to spread over the side walls (i.e., at $y = 1$ and $y = H$), which would result in the upward motion of the parcel of A fluid. A body force is applied in the negative z

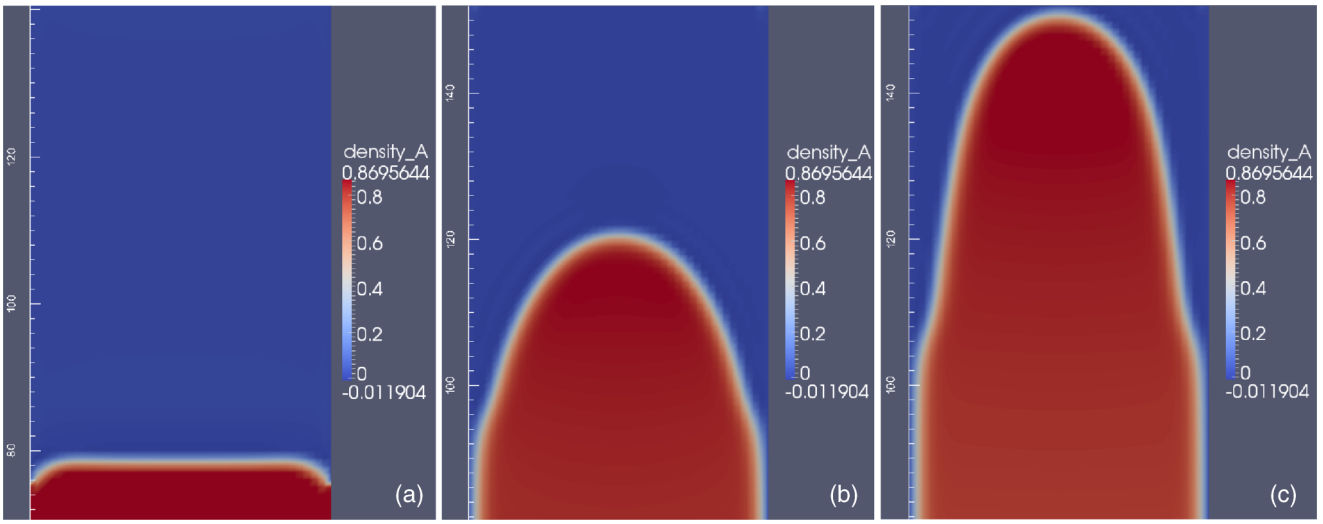

FIG. 6. Fluid flow through a channel at different times for the cases where each phase has a distinct n_s value ($n_s^A = 0.0$ and $n_s^B = 0.3$). (a) $t = 0$, (b) $t = 140$, (c) $t = 280$.

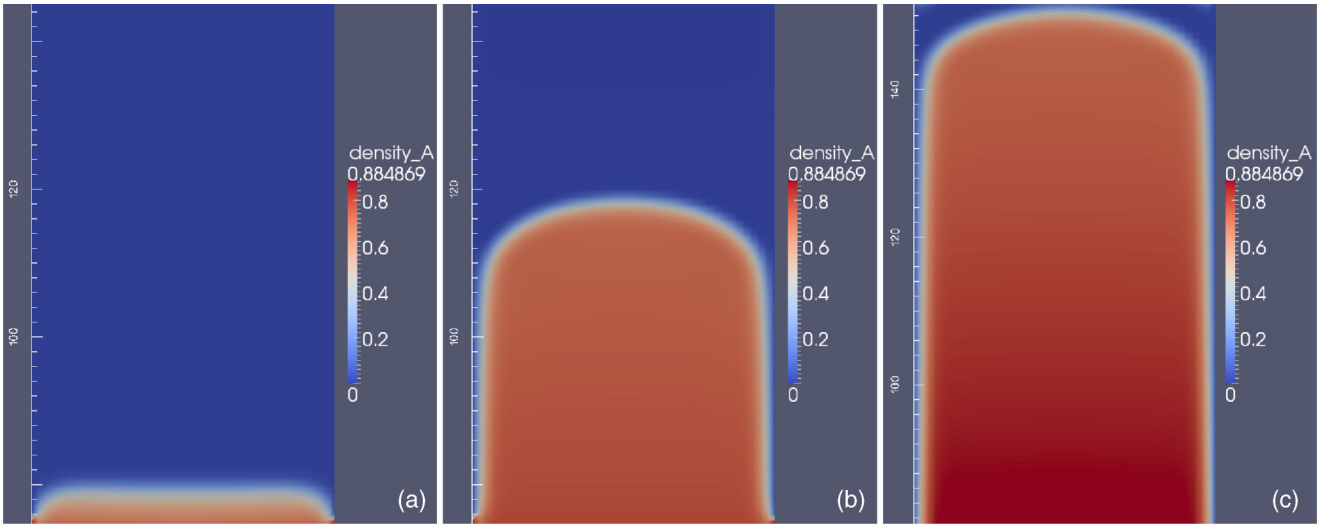

FIG. 7. Fluid flow through a channel at different times for the cases where each phase has a distinct n_s value ($n_s^A = 0.3$ and $n_s^B = 0.0$). (a) $t = 0$, (b) $t = 250$, (c) $t = 500$.

direction, which will oppose upward motion of the A phase. We use a body force of $G = 1.36 \times 10^{-6}$.

Figures 8(a)–8(c) show the progress of volume of A phase fluid at three different instants. Initially the A phase begins at the bottom of the channel and due to the attraction between this phase and the side walls it forms an acute angle with the wall. At the very bottom it can be noticed that the A phase is moving away from the bottom ($z = 0$) surface. At the next snapshot the A phase has moved up about half the length of the channel. Note that the A phase remains on the y boundaries (at the bottom end of the channel) since there is effectively a no-slip boundary condition here and thus the B phase appears in the central, bottom region, which was initially occupied by the A phase. In the final snapshot the A phase has reached the top of the channel. We emphasize that even though the body force is in the negative z direction, the A phase rises through the channel due to the enhanced wetting interaction provided by the side walls, i.e., due to capillarity.

We next consider filling the void region from the previous simulation with a partial solid, i.e., $n_s = 0.05$ and $s_s = 0.05$. (Setting both n_s and s_s the same value effectively assumes the solid is uniformly distributed at each node.) This will have two effects on the motion of the A phase. First, because n_s is nonzero it will retard fluid flow, but on the other hand, the non-zero s_s value enhances upward fluid motion. In the limit that $n_s \to 1$ we could not get any motion of the fluid, as all the f_i's would be continuously bounced back. Figures 8(d)–8(f) show the progress of the fluid for this case. The general motion of the fluid is similar to Figs. 8(a)–8(c), but overall the fluid motion is retarded. Whereas in Figs. 8(a)–8(c) it took 68 LB times steps for the A phase to reach the top of the channel, in the present case it takes 82 LB time steps. We have also tried cases where $n_s = s_s = 0.1$ and once again, the fluid motion is retarded in comparison to the previous two cases. In fact in this case it takes 93 LB times steps for the A phase to reach the top of the channel.

TABLE I. Average channel speed for the four combinations of n_s^A and n_s^B simulated where fluid resistivity varies between the two phases.

n_S^A	n_s^B	Average channel speed
0.0	0.3	0.27
0.3	0.0	0.15
0.5	0.1	3.9×10^{-4}
0.1	0.5	8.3×10^{-4}

We now consider a second validation for the solid-fluid interaction model. In this test we consider the situation where fluid imbibes into a porous medium due to capillarity effects (a process known as imbibition [38]). Consider a cuboidal block (porous medium) with a fluid reservoir placed at the bottom end. In this case, we do not place solid walls at the y edges, but simply the same n_s and s_s values as the rest of the lattice nodes. For this test we use $g_{As} = 0$ and $g_{Bs} = 0.33$. Once again a body force is placed in the negative z direction ($G = 1.36 \times 10^{-6}$), which opposes the upward motion of the fluid. As above, at each node we assume that the n_s and s_s values are the same and we vary these values from zero (void) up to 0.5. In the case when $n_s = s_s = 0$ we get no motion of the fluid, which is expected since the body force opposes upward fluid motion and there is not attraction between the A phase and the porous medium (which in this case is void). We have run simulations for n_s and s_s at 0.1, 0.15, 0.2, 0.25, 0.3, 0.35, 0.4, and 0.5. For each of these cases (where n_s and s_s are nonzero) we ran two varaints: (i) where the value for each node is uniformly distributed between zero and the upper nonzero value and (ii) where the value for each node is simply the nonzero value.

(i). Uniformly distributed nodal values. Here a node value for n_s and s_s is uniformly distributed between zero and 0.1 (or 0.2, . . . ,0.5). For the last two cases (0.4 and 0.5) the fluid remains static (at the bottom of the domain). In the other cases, (0.1, 0.2, 0.25, 0.3, and 0.35) the fluid rises up the porous medium [see Fig. 9(a)] as a flat front, which is typical of these five cases when capillary forces are dominant. However, the

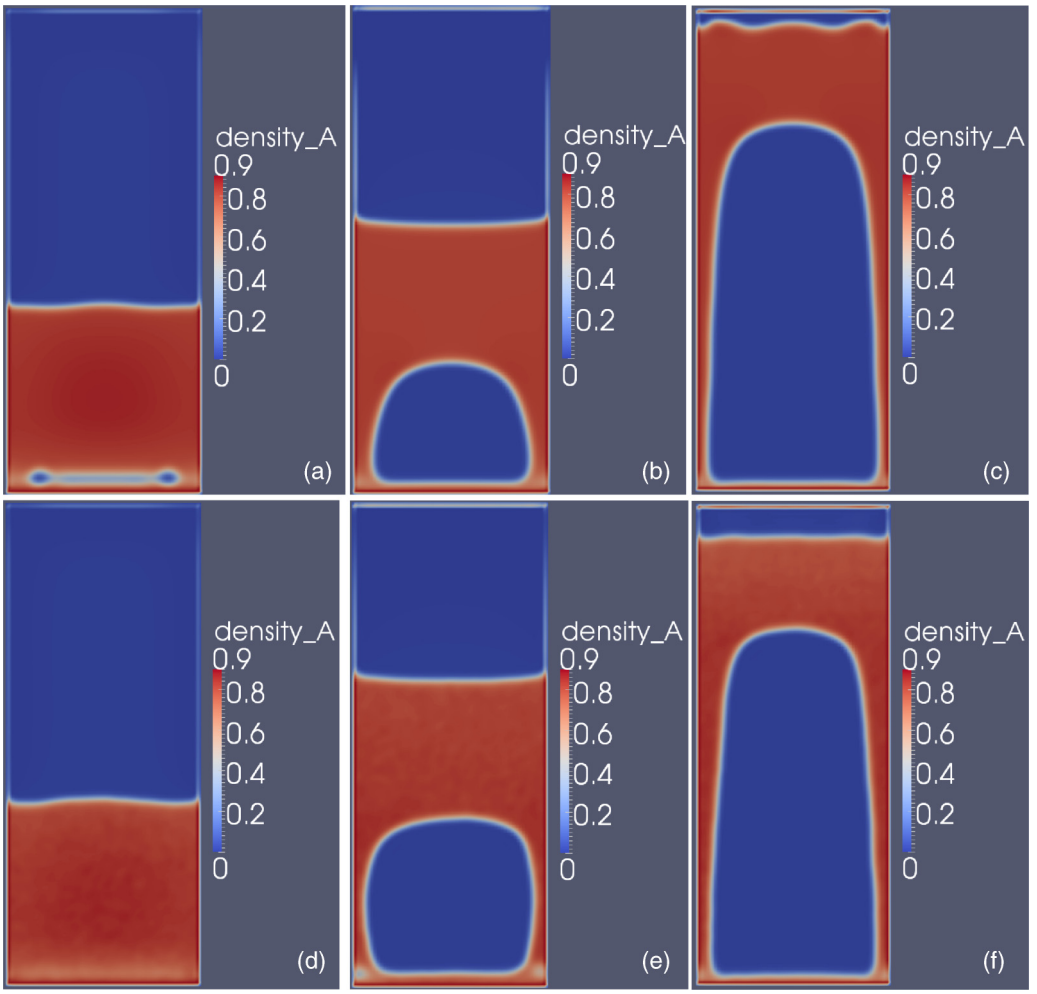

FIG. 8. Capillary rise in a channel due to an attractive interaction between the B phase (red) and walls. In the top row of figures $n_s = s_s = 0$ in the central region while in the bottom row $n_s = s_s = 0.05$. (a) Initial stages, (b) middle stages ($t = 30$), (c) final stages ($t = 69$), (d) initial stages, (e) middle stages ($t = 50$), and (f) final stages ($t = 82$).

time taken to reach the top is different for each case. In Fig. 9(b) we plot the average speed to reach the top of the channel and we see both for zero n_s and large n_s the speed is zero. In the former case there is no attraction between the porous medium (void) and fluid, while in the later case the medium resistance is too large for fluid to rise.

(ii). Same nodal values. Here all nodal values for n_s and s_s are the same. Again the case $n_s = s_s = 0$ results in no fluid rise for the same reason as above. However, the fluid stops rising up the porous medium at a much lower n_s value of around 0.2. Average speeds for the other cases (0.1, 0.15) are also plotted in Fig. 9(b) but now the window for capillary rise is much

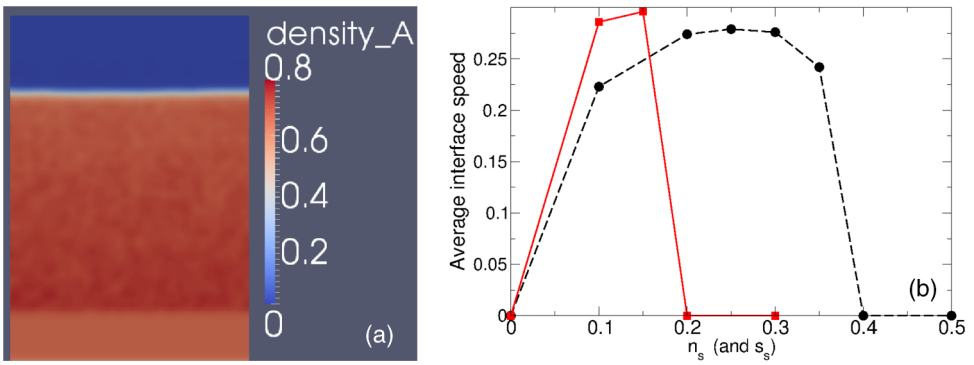

FIG. 9. (a) Snapshot of imbibition process in the middle stages. For all lattice nodes $n_s = s_s = 0.25$. The interface remains flat. (b) Average speed of interface versus n_s (or s_s). For the black squares the lattice n_s values are uniformly distributed between zero and the maximum (shown) n_s value while for the red circles all nodes have the same n_s value. Lines are drawn as a guide for the eye.

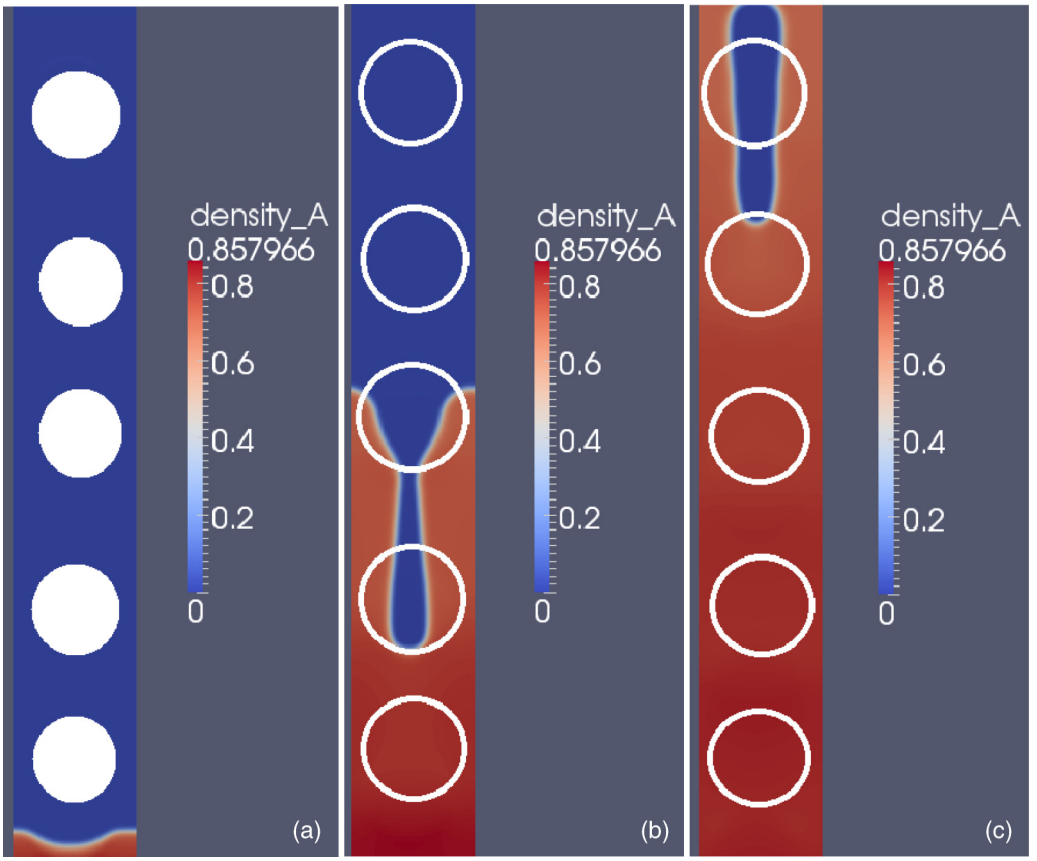

FIG. 10. Porous medium which consists of semipermeable tows (white discs), which have a larger n_s value than the surrounding region. The snapshots at various times are shown in the y-z plane. In (a) at $t = 100$ the invading phase (red) is at the bottom of channel and defending phase (blue) occupies the remainder. (b) At $t = 6000$ the invading phase flows around second tow, but has flowed completely filled the first tow. (c) At $t = 11000$ the invading phase bypasses the last tow. In (b) and (c) the tows have been superimposed on the images to show their approximate location.

narrower. When the node values (for n_s and s_s) are uniformly distributed, there are many nodes with a low n_s value. This provides lower resistance to fluid motion and hence a wider window for imbibition.

C. Flow in the presence of semipermeable structures

Given good agreement for channel flow between theory and the LB grayscale model we now proceed to consider flow around and through semipermeable cylindrical objects (tows), which have a higher resistance to flow than the surrounding medium. This case was previously considered by Spaid and Phelan [35] in the context of the Brinkman model. In these simulations the domain is periodic in all directions, but a body force is still applied in the z direction to generate fluid motion. The dimensions of the lattice is $21 \times 41 \times 701$ units. There are five cylindrical tows, which are spaced equidistantly apart [see white circles in Fig. 10(a)] with their axis parallel to the x direction. The tow regions are given an n_s value of 0.1 for the A phase and 0.0 for the B phase. Everywhere else both phases are given an n_s value of zero and periodic boundaries in all directions.

Figure 10 shows a slice in the y-z plane for the progress of the flood. Initially (time $t = 0$) the invading phase occupies the bottom part of the lattice (from $z = 1$ to $z = 310$). When the invading phase reaches a tow, the interface slows down. Since the tow region has a higher resistance for the invading phase, in the early stages the invading phase tends to flow around the tow [see Fig. 10(b)]. Eventually the invading phase does enter and flow through the tow, but at a much lower speed and so the interface takes on the shape of a necktie (bottom of necktie centers on the tow). Similar fluid motion occurs for flow around all subsequent tows. In the last snapshot [Fig. 10(c)], which shows the interface has passed the last tow, the front tips of the invading fluid coalesce. Eventually even this elongated region will be filled with invading fluid.

For this problem, Spaid and Phelan [35] have shown that the interface location, $\mathcal{R}(t)$, (between phases) can be predicted from Darcy's law as:

$$\mathcal{R}(t) = \frac{Gk}{\nu\rho\varepsilon}t, \tag{25}$$

where ε is the porosity given by $\varepsilon = 1 - \mathcal{V}_{\text{tow}}/\mathcal{V}$. Here $\mathcal{V}_{\text{tow}}$ is the volume of the tows and $\mathcal{V}$ is the total volume of the domain. We can track the interface between phases and plot it as a function of time (see Fig. 11). To calculate the interface position we take the average of three points on the interface, which are located on the left side ($y = 5$), in the center ($y = 20$), and on the right side ($y = 35$) of the channel. The data follows a line reasonably well, in agreement with Eq. (25),

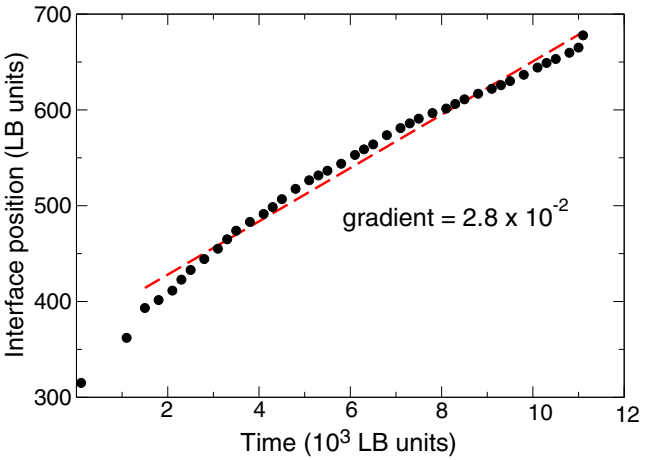

FIG. 11. Interface position versus time for the porous tow simulation shown in Fig. 10. Note the interface is initially located at $z = 310$. The red dashed line is a linear best fit to the beyond approximately 2×10^3 LB units.

although there are small deviations. These deviations are due to:

(i) the initial transition from zero velocity to steady-state conditions.

(ii) oscillations about the line due to the interface reaching a tow (where it slows down) and then after it passes the tow (where it speeds up).

Initially the invading fluid tends to pass relatively quickly through the low resistance region (region below tows). Once the interface reaches the tow the overall velocity of the invading fluid slows down. Eventually steady-state conditions are reached and the fluid velocity attains a constant value (albeit with small oscillations), as indicated by the linear fit to the data in Fig. 11.

D. Multiphase flow in real rock samples

The final scenario we consider is multiphase flow through real rock samples. These digital (CT) scans are of a CIPS (calcite *in situ* precipitation system) sandstone sample, which consists of calcite and quartz [23,36]. Each voxel is attributed a volume fraction of void (v_0) and calcite (v_c). Quartz is considered impermeable to fluid flow and calcite is partially permeable to fluid flow. As this is a demonstration of the capability of the new algorithm, we only use simple relationships connecting n_s and voxel compositions. Future work will consider more complex relationships, which model the underlying topology and composition more realistically. Hence, the effective n_s value for each voxel is determined according to the simple relationship

$$n_s = 1 - v_0 - p_c v_c, \tag{26}$$

where p_c is the effective percolating fraction of calcite [23]. This is an arbitrary variable, which can encompass a number of factors which may effect fluid flow in a voxel such as the solid fraction of calcite in the pore, distribution, topology and tortuosity of solid material, and possibly also the slip behavior. For this demonstration we consider a constant value of p_c for each voxel of 0.2. This also implies we keep the n_s value the same for each phase — in future work we will consider varying p_c in line with the factors just mentioned.

The sample consists of a $300 \times 480 \times 5$ voxel grid with a fluid reservoir at the $x = 0$ end (i.e., for $x < 0$). This simulation is a pseudo-three-dimensional simulation, as the thickness in the third dimension is very small. However, the advantage is that we can easily visualize and track the path of the invading phase through the sample. In addition, it allows us to complete a flood within a reasonable computation time.

The first flood we consider is at a low body force of $G = 6.8 \times 10^{-4}$ and four different snapshots are shown at various stages during the flood in Fig. 12. Note that because fluid can enter semipermeable regions we have overlaid the fluid (A phase density) on the underlying composition matrix to

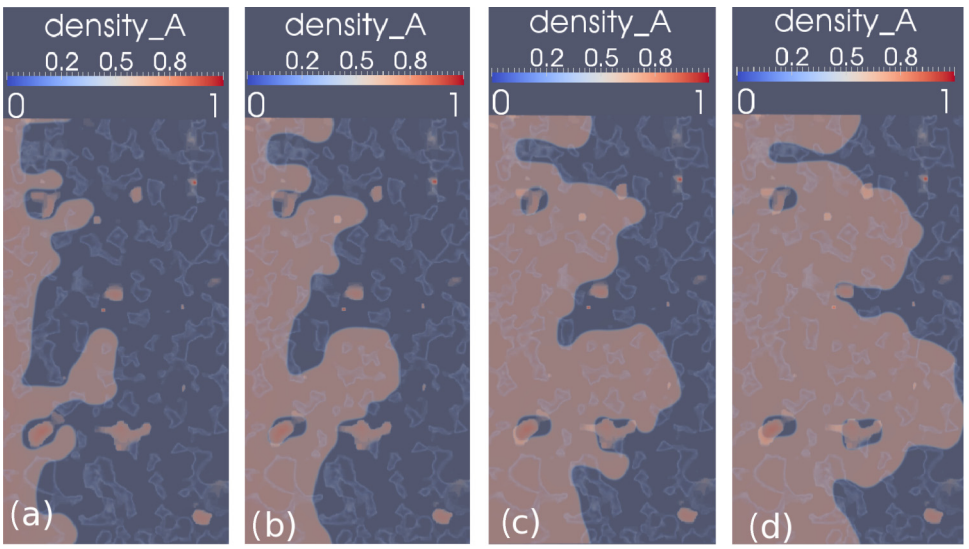

FIG. 12. Two-phase flood in the case of a real rock sample shown in the x-y plane at four different times for a body force (which is applied in the positive x direction, i.e., to the right) of $G = 6.8 \times 10^{-4}$. The invading phase fluid reservoir resides on the left edge of the domain. (a) $t = 5000$, (b) $t = 30000$, (c) $t = 50000$, (d) $t = 73000$.

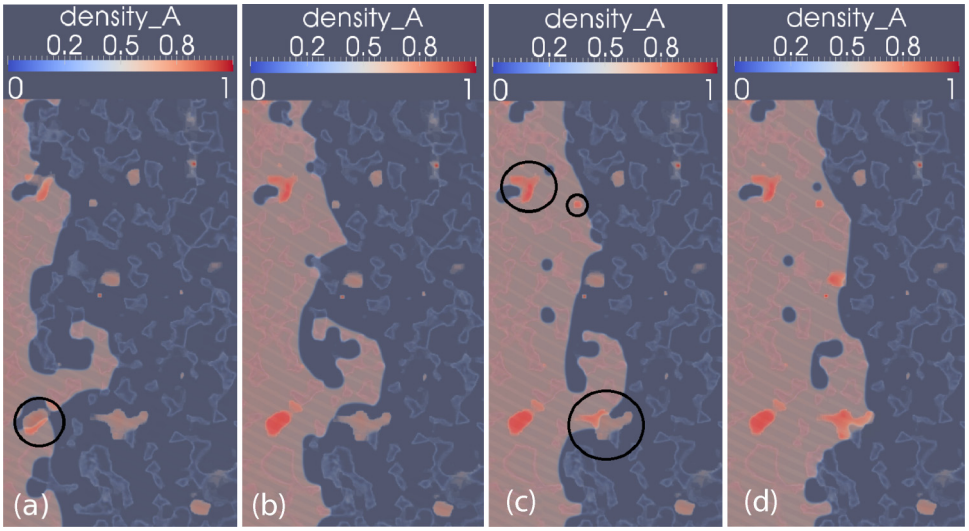

FIG. 13. Same flood as in Fig. 12 but with a solid-fluid attraction between the invading phase and solid. The invading phase fluid reservoir resides on the left edge of the domain. See the text regarding the circled regions. (a) $t = 5000$, (b) $t = 30000$, (c) $t = 50000$, and (d) $t = 73000$.

give the reader a perspective of where high n_s regions reside. In addition, these images contain all slices in the z direction (five in total), rather than just two-dimensional slices as in the previous figures. In Fig. 12(a) one can see both outlines of higher porosity regions and also isolated high-density clusters, which correspond to regions with large n_s values. The body force is applied in the positive x direction (i.e., towards the right in Fig. 12) and the injected phase begins on the left edge (reddish phase).

Early on [Fig. 12(a)] a number of fingers appear, which bypass the high composition regions in the sample. As time proceeds [Figs. 12(b) and 12(c)] the injected fluid tends to advance as a relatively wide but rough front, not entering the high composition regions. This can be seen by the grayish regions surrounding isolated cluster of orange-red. (Recall these isolated clusters of orange/red are in fact high fluid resistivity regions.) This advance is typical of capillary fingering where capillary forces dominate [37,38], i.e., injected phase advances by passing through largest pores or regions with lowest resistivity. In this case a relatively large amount of the injected phase invades the porous medium, which can be seen by the large amount of orange-red, which is present at breakthrough (Fig. 12d).

In the capillary flow regime, capillary forces (attraction between fluid and solid mineral) are important. Thus, we repeat the flood above but adding in an attractive interaction between the injected fluid and the solid. We use Eq. (24) for this interaction with $g_{As} = 0$ and $g_{Bs} = 0.33$ and for s_s at each node, we simply use the corresponding n_s value. Of course this need not be the case, but for this preliminary test we use this simple assumption. Figure 13 shows progress of the flood at similar times to Fig. 12. The most noticeable overall difference is that the flood is much slower. By 73000 LB time steps the fluid front is only (roughly) one-half to two-thirds of the distance to the exit. In Fig. 13(a) one can see the fluid enters the domain at roughly the same points. The higher n_s cluster in the middle of the domain (circled) is initially bypassed but by the next frame (at 30000 LB time steps) this cluster is surrounded and invaded. This is no doubt due to the attraction between fluid and solid, since this cluster is not invaded in Fig. 12. By 50000 LB time units, it becomes clear other high n_s clusters (circled) are invaded, whereas previously these remaind relatively untouched by the invading fluid. Overall by 73000 LB time steps the fluid front is relatively flat. Clearly the effect of the additional attractive interaction between fluid and solid tends to slow down the fluid front due to invasion of higher n_s regions.

The third flood we consider is at a higher body force of $G = 6.8 \times 10^{-3}$ and again four different snapshots at various stages are shown in Fig. 14. At this larger body force the invading front now resembles long fingers, which are primarily directed along the body force direction. Now that the fluid motion is dominated by the body force it tends to take the shortest pathway from inlet to outlet. Once again the high composition regions are bypassed and breakthrough is achieved much earlier than in the previous case, i.e., at $t = 4300$ compared to $t = 73000$ at the lower body force. Conjugate with this earlier breakthrough is a much smaller amount of defending phase, which has been invaded, indicated by a (comparatively) small amount of orange-red in Fig. 14(d). This flood is indicative of viscous fingering where the front takes the appearance of sharp, random fingers. This flood was carried without any solid-fluid interaction. In the case of viscous fingering, we argue these interactions are not important.

These cases demonstrate the correct physical dependence on flow rate (or body force), i.e., transition from capillary to viscous fingering. We can therefore be confident in the multiphase, grayscale method's capacity to model real physical phenomena. The next steps along this path is to apply the method to three-dimensional samples where the third dimension (z in this case) is comparable to the other two. Then a more complex topology of the medium results and can lead to much more interesting behavior than this pseudo-three-dimensional model. Most importantly in three dimensions, relative permeability curves can be constructed where each phase may have a nonzero permeability. In the cases we have

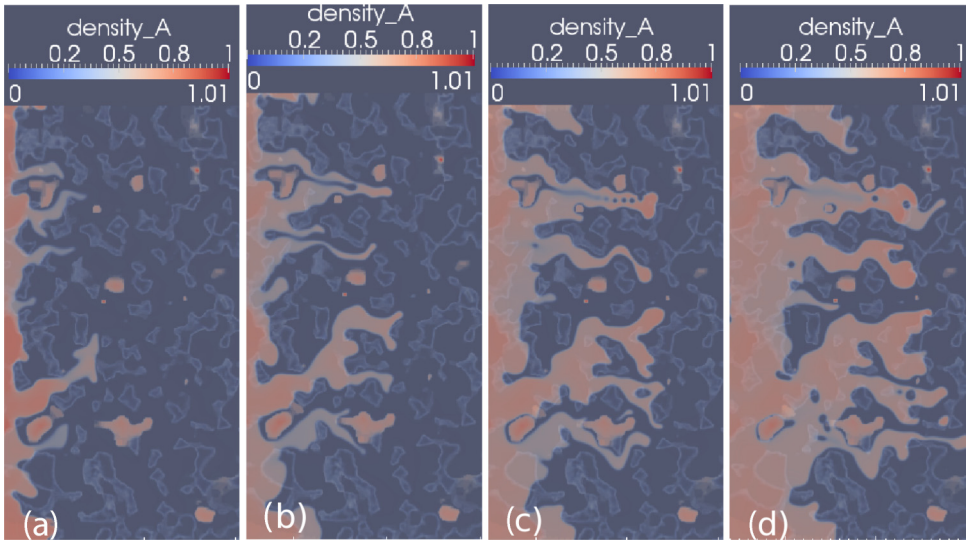

FIG. 14. Two-phase flood in the case of a real rock sample shown in the x-y plane at four different times for a body force (which is applied in the positive x direction, i.e., to the right) of $G = 6.8 \times 10^{-3}$. The invading phase resides on the left edge of the domain. (a) $t = 500$, (b) $t = 1400$, (c) $t = 2600$, (d) $t = 4300$.

just demonstrated once breakthrough is achieved the defending phase becomes (more or less) disconnected from inlet to outlet and therefore its permeability becomes zero.

IV. CONCLUSIONS

In this study we have developed and demonstrated the capability of a multiphase grayscale LB algorithm for modeling fluid flow in heterogeneous porous media. This method is based on a partial bounce back at each lattice node, where the degree of bounce back is related to the parameter n_s. While this parameter may depend on the solid fractions of each mineral that is present at a particular voxel, it should not be thought of as only dependent on this. It can also have contributions from how the solid phase is distributed in each voxel, i.e., topology and tortuosity as well as different mineral's surface slip (with various fluid phases), which may make up the voxel.

We have proposed a new algorithm and validated it on different test cases, which has shown it to be quite accurate and robust. Flow through a channel with different n_s values demonstrated that the interface between phases becomes less curved with increasing n_s. The velocity of the injected phase was found to be in agreement with a simple theory based on a model of Walsh *et al.* [18]. We have also shown that when each phase had a different n_s value, the model was numerically stable and yielded physically correct behavior. The most interesting case is the application of the model to real porous media. The results were qualitatively correct in that the flood changed characteristics from capillary fingering to viscous fingering with increasing body force.

For a multiphase problem, each phase can have a different n_s value and future work will consider implementing different dependencies of n_s on various factors, as mentioned above, and comparing these results. In situations where the solid-fluid interaction was applied, we assumed that the s_s value was the same as the n_s value. This need not be the case and in future we will investigate in detail different combinations of these parameters. We also will look at applying the model to large, cubical porous media samples and obtaining realistic relative permeability curves. The present model should be of great use in cases where the porous medium has a variety of minerals present where each mineral may have different resistivity (or slip) to a range of fluids. By having a method where each phase can independently have its own n_s value we should be able to model a wider range of multiphase flows in real rocks.

ACKNOWLEDGMENT

I would like to thank Dr. Paul W. Cleary for a detailed reading and comments on the manuscript.

[1] S. Succi, *The Lattice Boltzmann Equation for Fluid Dynamics and Beyond* (Oxford Science, New York, 2001).
[2] S. Chen and G. D. Doolen, Annu. Rev. Fluid Mech. **30**, 329 (1998).
[3] S. Succi, E. Foti, and F. Higuera, Europhys. Lett. **10**, 433 (1989).
[4] B. Ferréol and D. Rothman, Transp. Porous Media **20**, 3 (1995).
[5] C. Manwart, U. Aaltosalmi, A. Koponen, R. Hilfer, and J. Timonen, Phys. Rev. E **66**, 016702 (2002).
[6] M. G. Schaap, M. L. Porter, B. S. B. Christensen, and D. Wildenschild, Water Resour. Res. **43**, W12S06 (2007).
[7] T. Ramstad, N. Idowu, C. Nardi, and P. E. Oren, Transp. Porous Media **94**, 487 (2012).
[8] G. Jin, T. W. Patzek, and D. B. Silin, Paper SPE 90084, presented at the annual SPE conference and exhibition, Houston, Texas, 26–29 September, 2004.
[9] C. Chen, D. Hu, D. Westacott, and D. Loveless, Geochem. Geophys. Geosystems **14**, 4066 (2013).

[10] J. Yao, H. Sun, D. Fan, C. Wang, and Z. Sun, Pet. Sci. **10**, 528 (2013).
[11] J. Liu, G. G. Pereira, and K. Regenauer-Lieb, J. Geochem. Expl. **144**, 84 (2014).
[12] L. Chen, L. Zhang, Q. J. Kang, J. Yao, H. S. Viswanthan, J. Yao, and W. Q. Tao, Sci. Rep. **5**, 8089 (2015).
[13] L. Chen, W. Fang, Q. Kang, J. De'Haven Hyman, H. S. Viswanathan, and W.-Q. Tao, Phys. Rev. E **91**, 033004 (2015).
[14] K. Balasubramanian, F. Hayot, and W. F. Saam, Phys. Rev. A **36**, 2248 (1987).
[15] Y. Gao and M. M. Sharma, Transp. Porous Media **17**, 1 (1994).
[16] O. Dardis and J. McCloskey, Phys. Rev. E **57**, 4834 (1998).
[17] D. T. Thorne and M. C. Sukop, Dev. Water Sci. **55**, 1549 (2004).
[18] S. D. C. Walsh, H. Burwinkle, and M. O. Saar, Comput. Geosci. **35**, 1186 (2009).
[19] S. D. C. Walsh and M. O. Saar, Phys. Rev. E **82**, 066703 (2010).
[20] J. J. Zhu and S. Ma, Adv. Water Res. **56**, 61 (2013).
[21] I. Ginzburg, Adv. Water Res. **88**, 241 (2016).
[22] I. Ginzburg, G. Silva, and L. Talon, Phys. Rev. E **91**, 023307 (2015).
[23] R. Li, Y. S. Yang, J. Pan, G. G. Pereira, J. A. Taylor, B. Clennell, and C. Zou, Phys. Rev. E **90**, 033301 (2014).
[24] Y. S. Yang, A. Tulloh, F. Chen, C. Chu, and J. A. Taylor, DcmLite Software, CSIRO Data Access Portal, doi: 10.4225/08/53F6D60E7D48D.
[25] X. Shan and H. Chen, Phys. Rev. E **47**, 1815 (1993).
[26] M. L. Porter, E. T. Coon, Q. Kang, J. D. Moulton, and J. W. Carey, Phys. Rev. E **86**, 036701 (2012).
[27] M. Sbragaglia, R. Benzi, L. Biferale, S. Succi, K. Sugiyama, and F. Toschi, Phys. Rev. E **75**, 026702 (2007).
[28] X. Shan, Phys. Rev. E **73**, 047701 (2006).
[29] G. G. Pereira, in *Progress in Applied CFD*, edited by J. E. Olsen and S. T. Johansen, (Sintef Academic Press, Oslo, 2015), pp. 231–237.
[30] L. Chen, Q. Kang, Y. Mu, Y. L. He, and W. Q. Tao, Phys. Int. J. Heat Mass Trans. **76**, 210 (2014).
[31] X. He, S. Chen, and G. Doolen, J. Comput. Phys. **146**, 282 (1998).
[32] D. D'Humieres, I. Ginzburg, M. Krafczyk, P. Lallemand, and L.-S. Luo, Philos. Trans. R. Soc. London A **360**, 437 (2002).
[33] Z. Guo and T. S. Zhao, Phys. Rev. E **66**, 036304 (2002).
[34] Q. J. Kang, D. X. Zhang, and S. Y. Chen, Phys. Rev. E **66**, 056307 (2002).
[35] M. A. A. Spaid and F. R. Phelan, Composites **29A**, 749 (1998).
[36] R. R. Li, C. Chu, Y. S. Yang, and G. Pereira, DCM plugin for partially percolating LBM single phase flow, CSIRO Data Access Portal, doi: 10.4225/08/53F6E72A0D35E, 2014.
[37] R. Lenormand, E. Touboul, and C. Zarcone, J. Fluid. Mech. **189**, 165 (1988).
[38] G. G. Pereira, Phys. Rev. E **59**, 4229 (1999).